Figure 10 Photograph of the manufactured antenna

REFERENCES

1. Y. Zhang, Design of tri-band (EGSM/GPS/PCS) antenna with parasitic element for mobile phone application, Microwave Opt Technol Lett 48 (2006), 1347–1350.
2. J. Wen, C.R. Lin, and J.H. Lu, A planar meander-line antenna for triple-band operation of mobile handsets, Microwave Opt Technol Lett 41 (2004), 380–385.
3. E. Lee, P.S. Hall, and P. Gardner, Dual-band folded monopole/loop antenna for terrestrial communication system, Electron Lett 36 (2000), 1990–1991.
4. K.D. Katsibas, C.A. Balanis, A.A. Tirkas, and C.R. Birtcher, Folded-loop antenna for mobile handheld units, IEEE Trans Antennas Propag 46 (1998), 260–266.
5. H. Morishita, Y. Kim, Y. Koyanagi, and K. Fujimoto, A folded-loop antenna system for handsets, 2001 IEEE AP-S Int Symp Dig (2001), Boston, MA, 440–443.
6. P.L. Teng and K.L. Wong, Planar monopole folded into a compact structure for very-low-profile multiband mobile-phone antenna, Microwave Opt Technol Lett 33 (2002), 22–25.
7. D.M. Pozar, Microstrip antennas, Proc IEEE 80 (1992), 79–91.
8. K.L. Wong and L.P. Yang, Modified planar inverted F antenna, Electron Lett 34 (2002), 84–86.
9. S. Qu and C. Ruan, Effect of round corners on bowtie antennas, Progress In Electromagnetics Research, PIER 57 (2006), 179–195.
10. A.A. Abdelaziz, Bandwidth enhancement of microstrip antenna, Progress In Electromagnetics Research, PIER 63 (2006), 311–317.

CHARACTERIZATION OF MICROSTRIP TRANSMISSION LINES AT IR FREQUENCIES—MODELING, FABRICATION AND MEASUREMENTS

Tasneem A. Mandviwala,[1] Brian A. Lail,[2] and Glenn D. Boreman[1]
[1] College of Optics and Photonics, CREOL & FPCE, University of Central Florida, 4000 Central Florida Blvd., Orlando, FL 32816
[2] Department of Electrical and Computer Engineering, Institute of Technology, Melbourne, FL 32901; Corresponding author: blail@fit.edu

ABSTRACT: *We report the complete characterization of microstrip lines at an infrared frequency of 28.3 THz (10.6-μm wavelength) through modeling, fabrication, and measurement. The transmission-line parameters of interest can not be directly measured at infrared frequencies—the only measurable quantity is the voltage response of the antenna-coupled bolometric sensor. We validate the computational approach for transmission-line parameters by verifying the computed and measured response of the antenna connected to microstrip lines of different lengths. This also allows us to extend these calculations to explore various configurations and identify design trends. © 2008 Wiley Periodicals, Inc. Microwave Opt Technol Lett 50: 1232–1237, 2008; Published online in Wiley InterScience (www.interscience.wiley.com). DOI 10.1002/mop.23344*

1. INTRODUCTION

Metallic wire transmission lines have been extensively studied at radio frequencies (RF) [1–3] and millimeter wave frequencies [4–6]. At optical frequencies, dielectric waveguides are commonplace [7, 8] but metallic transmission lines have not been reported. In the course of development of phased-array antennas in the infrared (IR) band, we have selected metallic transmission lines as a baseline design due to the convenience of planar fabrication and potential for direct integration of the corporate feed structure with the antennas. In order to make proper use of these transmission lines in the design process, their characteristics must be computed and validated. To perform this investigation, we connect a single dipole antenna to a bolometer sensor [9, 10] through the transmission line. The bolometer is a temperature-dependent resistor, and its response is proportional to the power absorbed in it. At IR frequencies, this response represents the only experimentally measurable quantity. The desired transmission-line parameters must be developed in terms of this response, to allow for validation.

The design of transmission lines at IR frequencies requires taking into account material effects that can be neglected at RF. In the IR, the materials tend to be lousier and the propagation of THz-frequency current waves is affected by the large complex permittivity of the metal [11]. The propagation mode is hybrid, the signal distortion is high, and the attenuation is expected to be significantly influenced by radiative losses at these frequencies [12–14]. Thus, transmission lines at IR have unique attenuation and dispersion issues. Thus, the usual analytic formulas for computing transmission-line parameters that use quasi-static assumptions (valid below few hundred GHz), are not applicable in the IR.

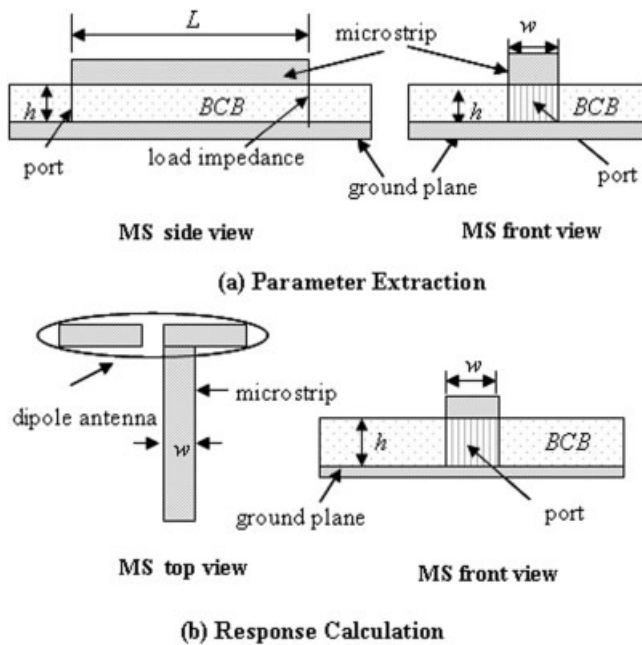Tasneem Mandviwala is currently at 3225 Woodland Park Dr, No. 1751, Houston, TX 77082.

Figure 1 HFSS models for parameter extraction and response calculation

For this reason, numerical modeling is necessary for characterization of transmission lines at IR frequencies. Using Ansoft HFSS, a full-wave finite-element method (FEM) electromagnetic solver, we compute the impedance at a defined port, based on the reflected and transmitted fields at the port. The transmission-line parameters of interest are obtained by curve-fitting this computed impedance to the impedance transformation equation as explained in section 2. We use measured IR-material parameters for the metals and dielectrics, obtained from IR variable-angle spectroscopic ellipsometry.

We characterize the transmission-lines using the following procedure [15]: (1) extract the transmission-line parameters: Z_o, α, and n_{eff} through numerical modeling; (2) compute the response of the antenna connected to the sensor through the transmission line as a function of line length; (3) fabricate the same antenna connected to transmission line of several lengths and measure the sensor response as a function of transmission-line length; and 4) compare the measured and modeled response. The response depends on the transformation of antenna impedance along the transmission-line length according to the transmission-line parameters of the specific line. Hence, verifying the computed response by comparison with the measured one validates the extracted transmission-line parameters. Although this procedure is similar to the one used for coplanar striplines in Ref. 15, in this work the responses are more accurately measured using F/1 optics.

2. NUMERICAL MODELING

Various methods of transmission line analysis may be broadly divided into three groups: (1) quasi-static methods, (2) dispersion models, and (3) full-wave analysis. Our approach is to use the full-wave FEM electromagnetic solver Ansoft HFSS to analyze the transmission lines. The complex material parameters used in HFSS are those actually measured at the IR frequency of interest using ellipsometry. Lumped port is used for excitation. Radiation boundary conditions are used for the outermost boundary of the model, essentially expanding the boundary infinitely far away from the structure by absorbing the outgoing wave. The load impedance used in the models for characterizing transmission lines was assigned from a lumped RLC boundary condition. The parametric sweep option in HFSS was the most convenient method for characterizing different transmission-line designs.

2.1. Parameter Extraction

Our procedure for extracting transmission-line parameters is based on parametric analysis of the transmission line as a function of its length. From full-wave field solutions, we compute the impedance at a defined port which is based on the reflected and transmitted fields at the port. This approach does not involve the use of analytical equations for computing transmission-line parameters, and hence, is a valid approach at IR. Our calculations are performed at 28.3 THz (10.6 μm), and yield the transmission-line parameters of characteristic impedance (Z_o), attenuation constant (α) and effective index of refraction (n_{eff}). Our model for extracting transmission-line parameters [(Fig. 1 (a)] consists of the transmission line connected to load impedance Z_L, (which represents the antenna), at one end, while the other end is connected to the port excitation (which represents the bolometer in the fabricated device). We extract the parameters in two steps as follows: (1) compute the input impedance at the port as a function of transmission-line length L and (2) fit the impedance versus transmission-line length curve thus obtained to the impedance transformation of Eq. (1):

$$Z_{in} = Z_o\left(\frac{Z_L \cosh(\gamma L) + Z_o \sinh(\gamma L)}{Z_o \cosh(\gamma L) + Z_L \sinh(\gamma L)}\right) \quad (1)$$

$$\gamma = \alpha + j\beta \quad (2)$$

$$\beta = \frac{2\pi}{\lambda_{eff}} \quad (3)$$

$$\lambda_{eff} = \frac{\lambda_o}{n_{eff}} \quad (4)$$

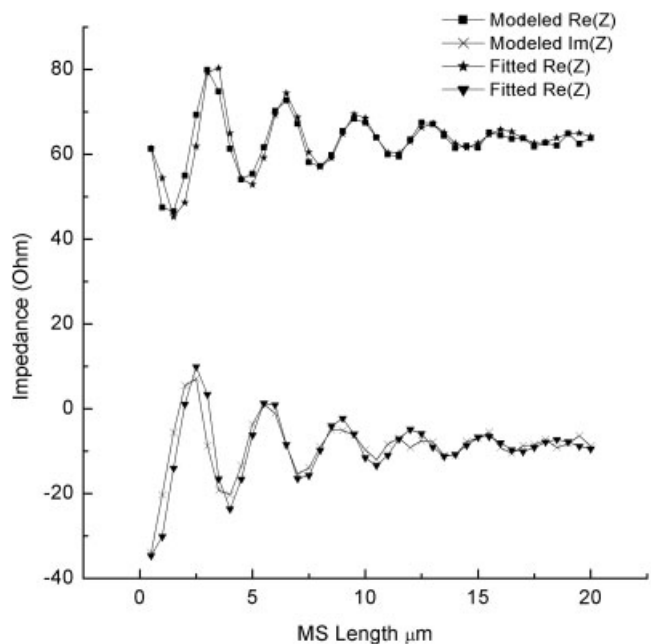**Figure 2** Curve-fitting of HFSS data to Eq. (1) for MS design consisting of $w = 0.4$ μm and $h = 0.2$ μm
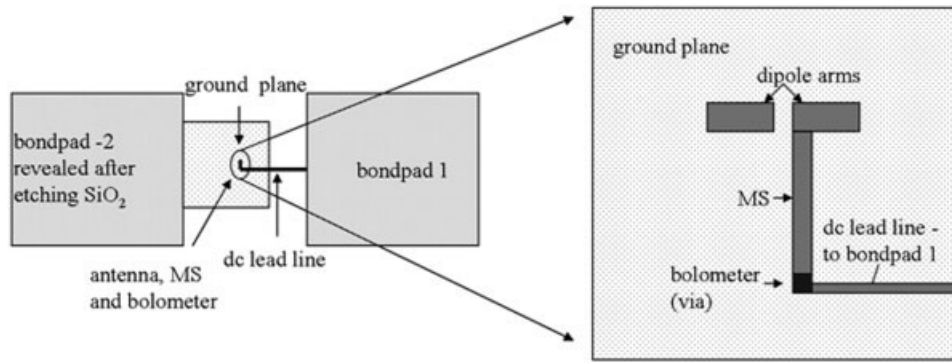
Figure 3 Top view of the MS device fabricated

where, Z_o is the characteristic impedance of the transmission line, Z_{in} is the input impedance at port end, β is the phase constant, λ_0 is free space wavelength, λ_{eff} and n_{eff} are the effective wavelength and refractive index, respectively, in the substrate. The parameters Z_o, n_{eff}, and α are found by fitting the impedance-transformation equation to the data obtained from HFSS by simultaneously varying these three unknowns. Each unknown has a particular effect on the Z_{in} versus transmission-line-length curve; e.g., the value of Z_o defines the peak of the curve, n_{eff} defines the spacing between peaks, while α defines the damping. We validated this computational approach for MS structures at 10 GHz using previously published transmission-line data from Refs. 16 and 17.

In our models, the MS substrate is a 200-nm-thick benzocyclobutene (BCB, also called cyclotene) layer backed by 200-nm-thick Au ground plane and a Si wafer as the underlying support. Figure 2 shows the impedance curve-fitting for MS design consisting of $h = 0.2$ and $w = 0.4$ and $Z_L = 100$ Ω. The extracted transmission-line parameters obtained from curve-fit are: $Z_o = 64$ Ω, $\alpha = 0.085$ Np/μm and $n_{eff} = 1.71$.

2.2. Response Calculation

In the models for parameter extraction, we connected one end of the transmission line to the lumped load (Z_L), and the other to the port. For the response calculation, we replaced the lumped load by a dipole resonant at 28.3 THz ($\lambda_0 = 10.6$ μm), as shown in Figure 1(b), and calculated the square of current at the port (response) as a function of MS length. This quantity is proportional to the I^2R power dissipated in the bolometer (where I is the current and R is the resistance of bolometer), and hence is directly comparable with the voltage response of the bolometer in the fabricated device. The computed normalized current-squared response is shown in Figure 6.

3. DEVICE FABRICATION

We fabricated dipole antennas connected to MS lines of lengths ranging from 0 to 11 μm in steps of 1 μm, on 200-nm-thick BCB backed by a finite ground plane (100 μm $\times$ 100 μm size). They were patterned using a Leica EBPG 5000+ electron-beam lithography system. These devices were fabricated on high resistivity Si wafers (resistivity: 4000–5000 Ω cm). As shown in Figure 3, the dipole antenna had two arms, each 1.4 μm in length and 0.6 μm in width, separated by a gap of 0.4 μm, hence making the total antenna length to be 3.2 μm. The dipole antenna was located above and in the center of the finite ground plane. The MS was located on the side of one of the dipole arms, towards the center of the dipole. The first layer in fabrication was the finite ground plane, a bondpad connecting the ground plane (bondpad 2 of Fig.

3) and alignment marks (not shown in the figure). These were all made of 200-nm-thick Au. The next step was to spin on the cyclotene [18] on this substrate. After coating the wafer with adhesion promoter (AP3000), BCB was spun at 3000 rpm and hard baked for 5 min on a hotplate at 250°C in nitrogen environment. We obtained the 200-nm-thick film of BCB by diluting 6022–38 series BCB in mesitylene solution with BCB to mesitylene ratio of 10:20.

The wafers were then coated with bi-layer e-beam sensitive resists: PMGI SF7 [19] and ZEP520A-7 [20], to pattern windows using e-beam lithography, for etching BCB to form bolometer and to etch open the bondpad 2 connected to ground plane. The bolometer was exposed using 15-nA beam current and the bondpad was exposed using 25-nA beam current with 120 μC/cm^2 dose for both. The two step development process consisted of first developing the exposed ZEP for 90 s in xylene (ZEP RD) and rinsing with IPA and then developing the PMGI for 20 s in tetra methyl ammonium hydroxide (TMAH) and rinsing with DI water. The samples were then put in the Plasma Therm reactive ion etching system to etch open the windows in the BCB [21]. The following process parameters were used: 50 mT chamber pressure, 10 sccm O_2, 5 sccm CF_4, 100 W RF power, and 280 V dc bias, giving an etch rate of 150 nm/min. The resist was removed using methylene chloride and EBR PG.

Next, the bolometer was patterned once again, for metallization, using the e-beam and development parameters mentioned
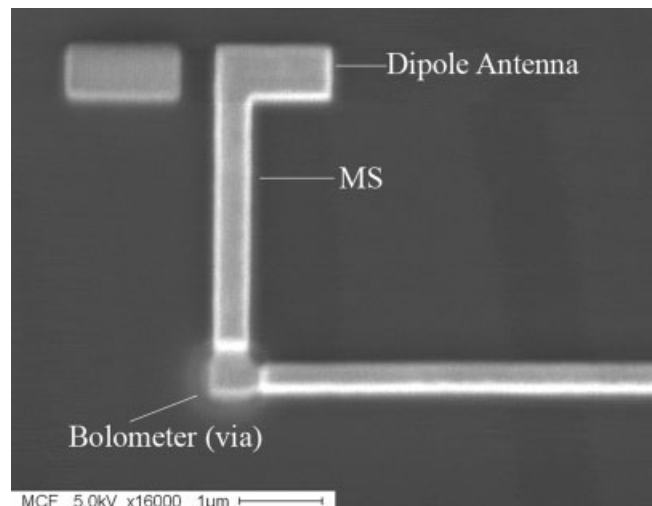

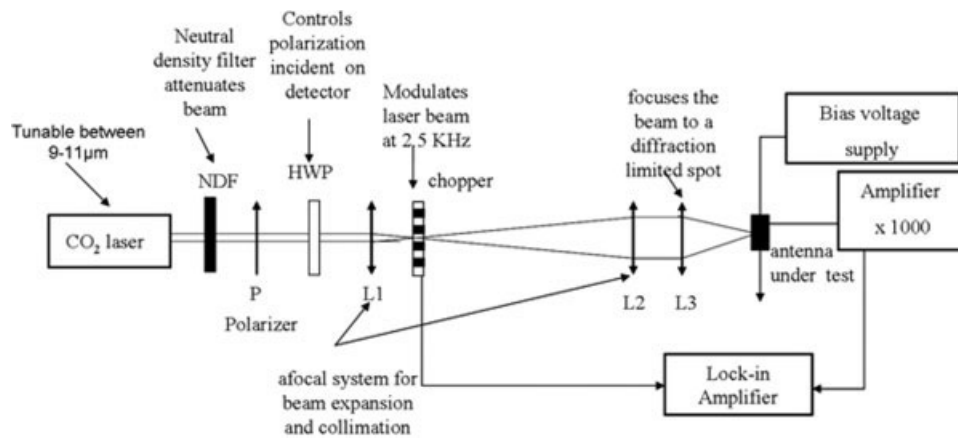**Figure 4** Fabricated dipole antenna connected to MS

Figure 5 Test setup for response measurement

above. It was metallized using e-beam evaporated 10–200-nm-thick Ti-Au. In the next step, the dipole antennas, microstrip lines, lead lines and the bondpads (bondpad 1) were fabricated on top of BCB. The antennas, MS and lead lines were patterned with 15-nA beam current and 120 μC/cm^2 dose and the bondpad was patterned with 25-nA beam current and 120 μC/cm^2 dose. They were developed in xylene and TMAH for 90 and 20 s, respectively and then metallized with e-beam evaporated Ti-Au (10–150 nm). A fabricated device is shown in Figure 4.

4. EXPERIMENTAL RESULTS

We measured the voltage response of the bolometer as a function of transmission line length. Other modeled parameters such as characteristic impedance, attenuation constant, and effective index cannot be measured directly. The only directly measurable quantity is the voltage response of the bolometer. So we compute, measure, and compare the response of the bolometer connected to the dipole antenna by these transmission lines as a function of transmission-line length. The measured response is proportional to the power dissipated in the bolometer and we compare this quantity with the current squared at the bolometer (port) computed from our model. This current depends on the impedance at bolometer (port) location which in turn is the impedance of the dipole antenna transformed along the line length based on transmission-line parameters and hence directly related to the computed Z_o, n_{eff}, and α of that particular design. Thus, our response measurement can be

related to the modeled transmission-line parameters and their validity can be confirmed.

The characterization of the devices was carried out using test setup shown in Figure 5. The measurements were performed with the CO_2-laser beam at 10.6 μm focused by an F/1 optical train producing the laser spot diameter of about 30 μm. The polarization was linear and was rotated by means of a half-wave plate to test the polarization sensitivity and to confirm the orientation of the dipole. The bolometer under test was biased at 100 mV and placed at the focus of the laser beam using motorized stages with submicron accuracy. The laser beam was modulated with a chopper at a frequency of 2.5 kHz and the modulated signal produced by the bolometer was read with a lock-in amplifier after a 1000× preamplification. When compared with the response measurements of Ref. 15, which used F/8 optics, this method was more accurate, where, for each device we obtained an antenna response map with a scan step size of 1 μm. As a result a 2D map of the response of antenna was obtained which represents the convolution between the detector's spatial response and the laser beam shape [22]. The 2D maps were recorded for each device to accurately obtain the response due to antenna and to distinguish between the bondpad response and antenna response.

Figure 6 show the measured normalized antenna response overlaid to normalized modeled response for MS and they are in good agreement indicating the validation of our modeled transmission-line parameters.
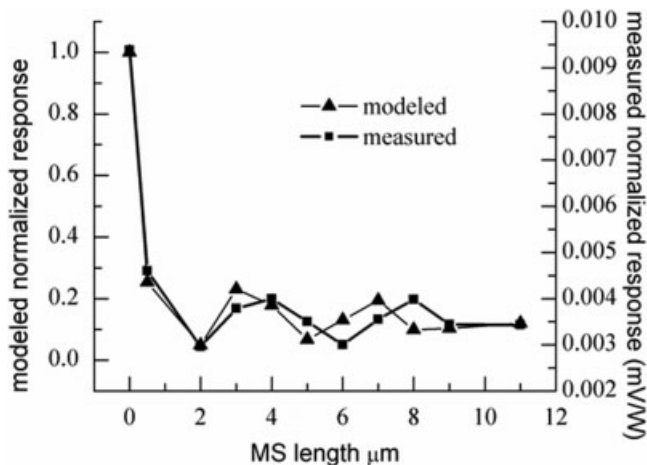

Figure 6 Comparison of measured and computed response for MS

TABLE 1

Optical Constants Measured from IR-VASE, at a Wavelength of 10.6 μm

Material	Thickness, h (nm)	N	k
Au	150	12.6	65.28
PECVD SiO$_2$	150	2.3496	0.12307
	200	2.0535	0.41285
	300	2.2824	0.293
BCB	200	1.547	0.0054
	260	1.542	0.0066
	330	1.528	0.022
ZrO$_2$	60	1.5795	0.02531
	80	1.530	0.0334
	470	1.4245	0.1058

Figure 7 Z_0 for MS on PECVD SiO_2, ZrO_2 and BCB as a function of w and h
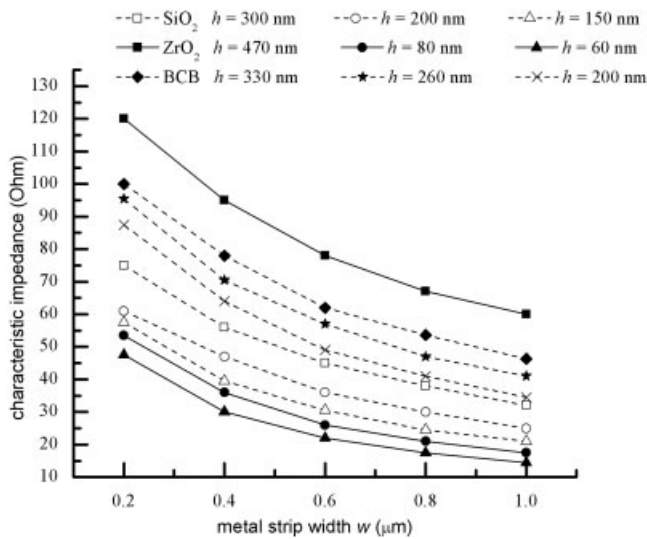

Figure 9 n_{eff} for MS on PECVD SiO_2, ZrO_2, and BCB as a function of w and h

5. PARAMETER EXTRACTION FOR DIFFERENT MS DESIGNS

After validating the characterization approach for MS, we ran a number of models with different MS substrates and studied the trends in the IR-transmission-line design variables. The MS structure was studied on (1) PECVD SiO_2, (2) ZrO_2, and (3) BCB. The models use actual material parameters measured at a wavelength of 10.6 μm using IR ellipsometry. The metal used is Au. The measured real and imaginary parts of refractive index, n and k, of each material are shown in Table 1. Knowing n and k, the permittivity and the conductivity are calculated, which are then used to assign a material in HFSS.

The MS structure has essentially two design variables: the metal strip width w and substrate thickness h. The metal strip width w for each substrate was varied between 0.2 and 1 μm in steps of 0.2 μm. Figures 7–9 show extracted parameters for MS lines as a function of h and w. We find that as w increases, the characteristic impedance decreases for all values of h, giving lowest values for the sm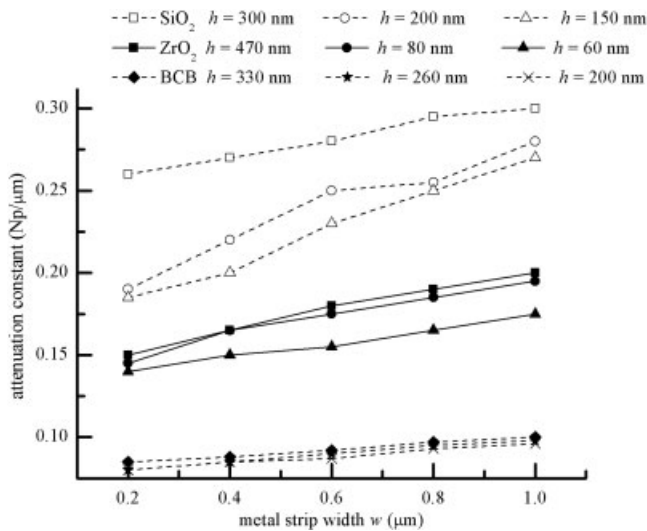allest h. The effective index of refraction is higher for thicker substrates and increases as a function of w. The attenuation constant is higher for thicker substrates and also increases with w.

In addition, we computed and compared the attenuation for MS and CPS configurations. Our simulation results show that for a given substrate material, the MS configuration has lower attenuation when compared with the CPS configuration. Figure 10 shows the attenuation plot for the MS and the CPS configurations on 200-nm BCB substrate as a function of strip width w.

6. CONCLUSION

A modeling procedure, fabrication process, and measurement results for MS transmission lines at LWIR were reported. Microstrip lines were characterized at a wavelength of 10.6 μm in the IR. We used a finite-element approach to compute characteristic impedance, attenuation constant, and effective index of refraction for these lines. The response of an antenna-coupled bolometer measured as a function of transmission-line length was found to agree closely with the response computed with transmission-line parameters extracted from the models, when measured values of IR-material properties were used. Design trends in terms of geometry
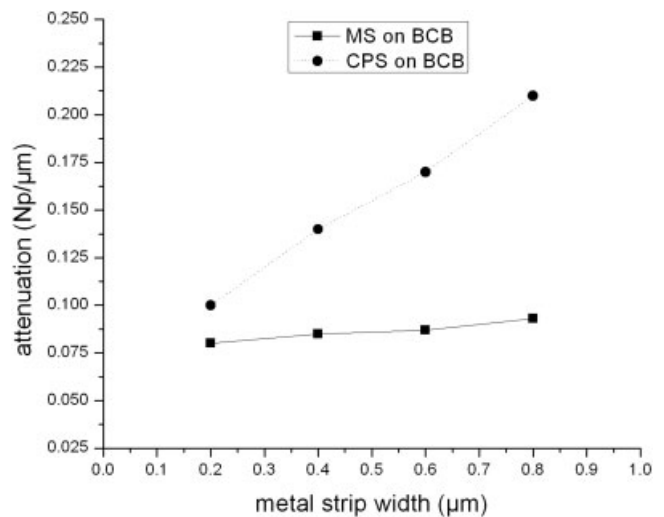

Figure 8 α for MS on PECVD SiO_2, ZrO_2 and BCB as a function of w and h

Figure 10 Attenuation for MS and CPS on 200-nm-thick BCB as a function of w

and materials were presented. The MS configuration was found to have lower attenuation than its CPS counterpart.

REFERENCES

1. H.A. Wheeler, Transmission line properties of parallel strips separated by a dielectric sheet, IEEE Trans Microwave Theory Tech 13 (1965), 172–185.
2. T. Itoh and R. Mittra, Spectral-domain approach for calculating dispersion characteristics of microstrip lines, IEEE Trans Microwave Theory Tech 21 (1973), 496–499.
3. T. Hatsuda, Computation of coplanar-type-strip line characteristics by relaxation method and its applications to microwave circuits, IEEE Trans Microwave Theory Tech 23 (1975), 795–802.
4. M. Abdel Rahman, B. Monacelli, A. Weeks, G. Zummo, and G.D. Boreman, Design, fabrication and characterization of antenna-coupled metal-oxide-metal diodes for dual-band detection, Opt Eng 44 (2005).
5. I. Jeong, S.-H. Shin, J.-H. Go, J.-S. Lee, C.-M. Nam, D.-W. Kim, and Y.-S. Kwon, High performance air gap transmission lines for millimeter wave applications, Microwave Symp Dig IEEE MTT-S Int 2 (2002), 661–664.
6. J.-H. Kim and D.-H. Han, Hybrid method for frequency-dependent lossy coupled transmission line characterization and modeling, In: Proceedings of Topical meeting on Electrical performance of Electronic Packaging, 2003, pp. 239–242.
7. N.S. Kapany, J.J Burke, and T. Sawatari, Fiber optics technique for launching an arbitrary mode on an optical dielectric waveguide, J Opt Soc Am 60 (1970), 1178.
8. A. Ortega-Moñux, J.G. Wangüemert-Pérez, and I. Molina-Fernández, Adaptive hermite-gauss decomposition method to analyze optical dielectric waveguides, J Opt Soc Am A 20 (2003), 557–568.
9. I. Codreanu and G. Boreman, Integration of microbolometers with infrared microstrip antennas, Infrared Phys Technol 43 (2002) 335–344.
10. F.J. González, M.A. Gritz, C. Fumeaux, and G.D. Boreman, Two dimensional array of antenna-coupled microbolometers, Int J Infrared Millimeter Waves 23 (2002), 785–797.
11. C. Fumeaux, M. Gritz, I. Codreanu, W. Schaich, F.J. González, and G. Boreman, Measurement of the resonant lengths of infrared dipole antennas, Infrared Phys Technol 41 (2000) 271–281.
12. D. Grischkowsky, I.N. Duling, III, J.C. Chen, and C.C. Chi. Electromagnetic shock waves from transmission lines, Phys Rev Lett 59 (1987), 1663–1666.
13. D.B Rutledge, D.P. Neikirk, and D.P. Kasilingham, In: K.J. Button (Ed.), Infrared and Millimeter waves, Vol. 10, Part 2, Academic Press, New York, 1983.
14. D.R. Grischkowsky, Optoelectronic characterization of transmission lines and waveguides by terahertz time-domain spectroscopy, IEEE Trans Select Top Quantum Electron 6 (2000), 1122–1135.
15. T. Mandviwala, B. Lail, G. Boreman, Infrared frequency coplanar striplines: Design, fabrication and measurements, Microwave Opt Technol Lett 47 (2005), 7–20.
16. K.C. Gupta, R. Garg, and I.J. Bahl, Microstrip lines and slotlines, Artech House, Norwood, MA, 1979.
17. I.J. Bahl and D.K. Trivedi, A designer's guide to microstrip line, Microwaves 16 (1977), 174–182.
18. Dow Chemical, CYCLOTENE™ 3000 Series Advanced Eclectronic Resins, The Dow Chemical Company, 2005. Available at http://www.dow.com/cycoltene/resource/prodlit.htm/.
19. Microchem, Nano PMGI Resists, Microchem Corp., Newton, MA, 2002. Available at http://www.microchem.com/products/pdf/pmgi_resist.pdf.
20. Zeon Corporation, ZEP520A Technical Report, ZEON Corp. Specialty Materials Division, 2003. Available at http://www.zeon.co.jp/.
21. M.J. Berry, P. Garrou, B. Rogers, and I. Turlik, Soft mask for via patterning in BCB dielectric, Int J Microcircuits Electron Packag 17 (1994), 210.
22. J. Alda, C. Fumeaux, I. Codreanu, J. Schaefer, and G. Boreman, A deconvolution method for two-dimensional spatial-response mapping of lithographic infrared antennas, Appl Opt 38 (1999), 3993–4000.

A NOVEL COMPACT DUAL-BAND BANDPASS FILTER USING ASYMMETRIC SIRS FOR WLANS

Yu-Chi Chang,[1] Chia-Hsiung Kao,[1] Min-Hang Weng,[2] and Ru-Yuan Yang[3]
[1] Department of Electrical Engineering, National Sun Yat-Sen University, Taiwan
[2] National Nano Device Laboratories, Taiwan
[3] Department of Material Engineering, National Pingtung University of Science and Technology, Taiwan; Corresponding author: ruyuan.yang@gmail.com

ABSTRACT: *In this article, a novel compact dual-band bandpass filter (BPF) using asymmetric stepped impedance resonators (SIRs) has been presented for the first time. The feature of the proposed asymmetric SIR is only one step discontinuity, which is different from the conventional SIR with two step discontinuities. The frequency response of the dual-band at 2.4/5.2 GHz can be achieved by determining the impedance ratio (K) and physical length ratio (α) of the asymmetric SIR. The coupling coefficient between the coupled asymmetric SIRs is calculated by using full-wave simulator IE3D. A dual band BPF is designed, fabricated, and measured. The measured results are in good agreement with the full-wave simulation results. Additionally, the BPF has a smaller circuit size in comparison of previous works.* © 2008 Wiley Periodicals, Inc. Microwave Opt Technol Lett 50: 1237–1240, 2008; Published online in Wiley InterScience (www.interscience.wiley.com). DOI 10.1002/mop.23339

1. INTRODUCTION

In recent year, there is a growing interesting for the wireless communication applications operating in multiband, especially in the new developed wireless local area network (WLAN) standards such as IEEE 802.11b/g (2.4 GHz) and IEEE 802.11a (5.2–5.8 GHz) specifications. In such mobile dual-band communication systems, planar microstrip dual-band bandpass filter (BPF) is always a key component of a RF receiver. Conventional stepped impedance resonator (SIR) consists of two step discontinuities, a central section of high (low) impedance and two sections of low (high) impedance in the end of the central section [1-11]. By shifting the higher order frequency of the SIRs to the desired second passband, dual-band BPFs have been implemented [2-8]. However, the dimensions of previous works are still large because the SIRs are arranged by the direct-coupling or cross-coupling structure, and the second passband of the above dual-band filters are still have higher insertion loss with about 3 dB or more than 3 dB because of the use of two step discontinuities [5-8].

In this article, a novel compact dual-band BPF using asymmetric SIRs with one step discontinuity for WLANs is proposed. By